The neutron source at the PTB is a berylium target, which is bombarded by deuterons of about 13.5 MeV. The nuclear reaction ^{9}Be(d,n)^{10}B provides a neutron field with a mean energy of $< E_n > = 5.3$ MeV and a rather high flux of up to $1.2 \cdot 10^{10}$ cm$^{-2}s^{-1}$ At the UKE facility deuterons on a tritium target ^{3}H(d,n)^{4}He provide monoenergetic neutrons ($E_n = 14.1$ MeV) having a maximum flux of $8.5 \cdot 10^8$ cm$^{-2}s^{-1}$. The maximum fluxes given above refer to a distance of 10 cm from the target.

The hardness factors of the neutron sources listed in tab. 5.2 were calculated using eq. 3.3. The spectrum of the berylium source is taken from [98]. Further details concerning the irradiation facilities can be found there and in [37] (PTB) and [99] (UKE). The main properties are compiled in tab. 5.2.

Facility	Reaction	Neutron Energy [MeV]	Hardness Factor κ	Neutron Flux † [cm^{-2}s^{-1}]	Error in Φ	γ-Background
PTB	^{9}Be(d,n)^{10}B	5.3 *	1.53	$1.2 \cdot 10^{10}$	$\leq$5%	5%
UKE	^{3}H(d,n)^{4}He	14.1	1.88	$8.5 \cdot 10^8$	$\leq$5%	$\leq$5%

Table 5.2: Survey of irradiation facilities († at a distance of 10 cm from target, * mean value)

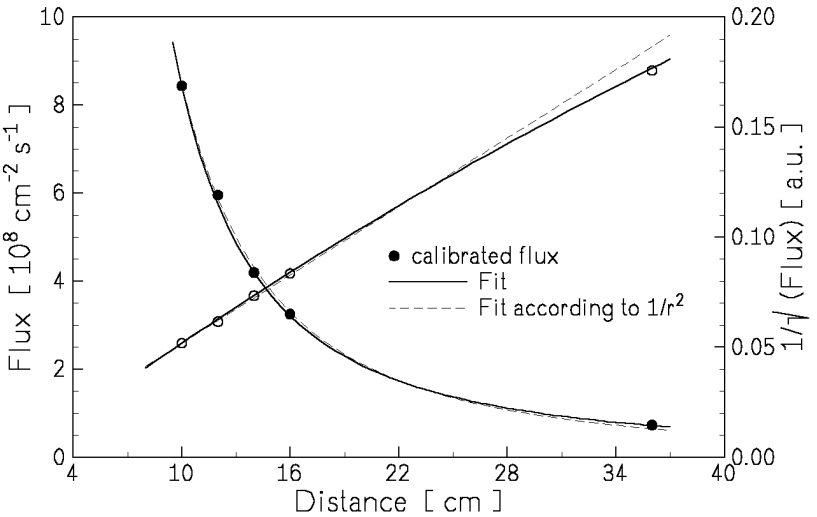

Figure 5.2: Flux as function of distance (r) as measured at the UKE facility. Fit used for calculation of fluence is according to $\Phi(r) = p_1/(p_2 + p_3 r + p_4 r^2)^2$. For comparison the r^{-2}-dependence is also shown.

Samples assigned for irradiation were mounted along the beam axis at various distances from the target. In order to determine the distance and time of exposure necessary to obtain the desired fluence, the flux was measured with a calibrated ionisation chamber at several positions. Fig. 5.2 shows the flux as function of distance

as measured at the UKE facility. The measured points were fitted to a function (see caption of fig. 5.2) taking into account the deviation from the r^{-2}-dependence. The fit was used then to calculate the flux for each sample position and the exposure time for a reference position could be estimated. During the exposure the neutron flux was monitored by a second calibrated ionisation chamber. Because of a well defined ratio of flux at the reference position and at the monitor chamber, the accumulated fluence at the reference position was monitored simultaneously. If the desired fluence was achieved, the exposure was stopped. This way an exact dosimetry was possible even if the beam intensity was fluctuating. The only source of error besides the uncertainty of the flux ($\leq$5%) was the measurement of the sample target distance. The accuracy of the measurement was always better than $\pm$ 1 mm, which results in a 2% error at 10 cm distance and less at greater distances. Thus a reasonable estimate on the error of fluence determination is 7%.

The techniques used to perform the low temperature irradiation experiments are described in sec. 5.4.

5.3 Measurement Set-Up

To perform IV- and CV-measurements at room temperature the samples were usually placed in a brass chamber or probe station, both being light-tight, electrically shielded and providing feed-throughs for cabling. The temperature was measured using a Pt-100 resistor. Measurements at lower temperature took place either in one of the cryostats or in the Peltier cooler, which are described in sec. 5.4.

The current-voltage characteristics were measured using either a pico-amperemeter *Keithley 485* (K485) in connection with a power supply EM 500 (or EM 50) from *Emetron* and a voltage meter *Keithley K175* or using the *Keithley K487*, which provides ampere-meter and controlled power supply in one apparatus. Both voltage sources are limited to 500 volts. The circuit diagram for the IV-measurement is shown schematically in fig. 5.3.

Also the CV-measurements were performed with two different set-ups. The capacitance was measured either using a lock-in amplifier *EG&G Parc 5210* or a capacitance-bridge, *Hewlett Packard 4263A* LCR meter (HP-bridge). While the lock-in amplifier was used in connection with the EM 500 and the K175, the K487 served as voltage source when the HP-bridge was used. Because the operation of the bridge is limited to voltages below 20 V, a special adapter was linked into the circuit to allow the application of higher voltages. The internal oscillator of the *Parc 5201* covers a frequency range from 50 Hz to 120 kHz and provides amplitudes from 5 mV to 2 V. In contrast the HP-bridge provides fixed frequencies 0.1, 0.12 1, 10, and 100 kHz and fixed amplitudes in the range of 50 mV to 2 V. Typically 10 kHz signals with an amplitude of 40 mV, or 0.5 V were applied. While the HP-bridge is calibrated absolutely, the out-put of the lock-in amplifier is an AC-signal, which has to be calibrated by the experimenter. A schematic of the circuit diagrams for the CV-measurements is shown in fig. 5.3.

Both, IV- and CV-measurements and also the DLTS- and TSC-measurements described in the following were controlled by a computer (PC) over a standard GPIB (IEEE) bus.

(a)

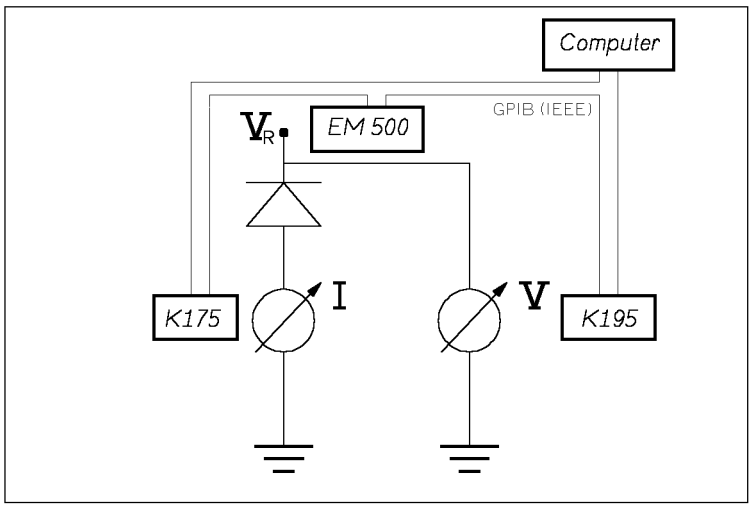

(b)

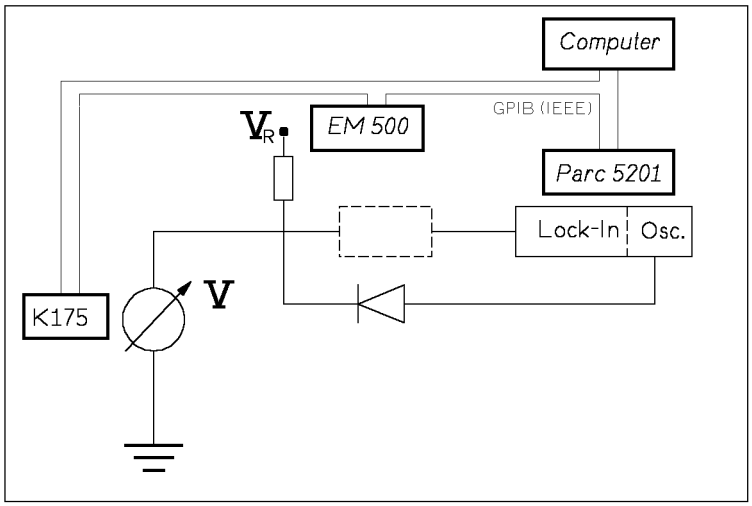

(c)

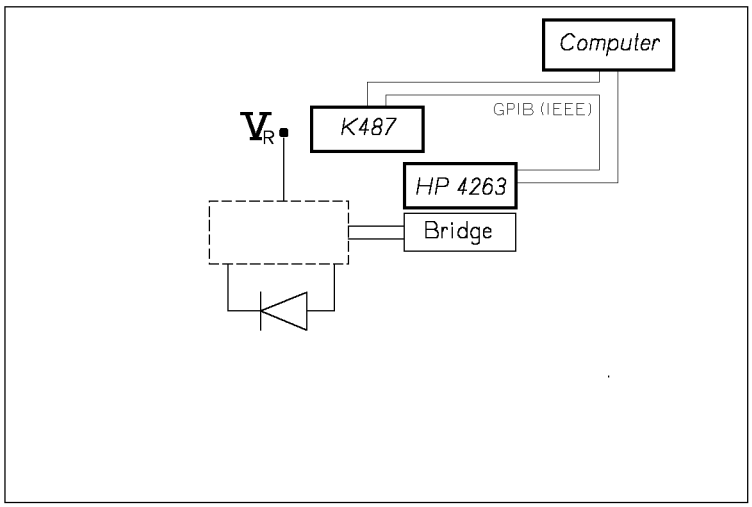

Figure 5.3: Schematic of circuit diagram. (a) IV-measurement, the circuit containing the K487 is not shown, because it looks very similar. (b) CV-measurement with the lock-in amplifier. (c) CV-measurement with the HP-bridge. The dashed boxes contain circuits to de-couple the high voltage from the bridge, respectively the lock-in amplifier.

The DLTS-system [3] consists of a capacitance bridge, a digital data acquisition system, a software package to control and analyse the measurements. A detailed description of the hardware and software is given in [85, 100]. The cryostats in use and the temperature controling unit are described in sec. 5.4. The 1 MHz capacitance brigde (*Boonton 72BD*) [101] Full scale ranges from 1 pF to 3000 pF can be chosen and the resolution is 0.5% of full scale on all ranges. However, due to an external capacitor which compensates for the capacitance of equilibrium only the change of the capacitance due to the emission process can be measured in the lowest full scale range, the equilibrium capacitance is suppressed. Depending on the averaging of the analog output signal a resolution of below 100 aF can be achieved [100, 102]. A rather short building-up time ($\approx$ 0.2 ms) enables the measurement of fast emission processes. The analog signal is filtered and then converted to a digital signal (resolution of ADC is 12 bit). The transient recorder allows a time binning of the signal into 2^n (n : 6 - 10) equidistant intervals of 0.02 ms to 3 s length. Usually 512 (n= 9) bins were used. The transients can be recorded repeatedly for subsequent averaging. The signal analysis (folding of the transient) is performed by the computer. The set-up is shown schematically in fig. 5.4.

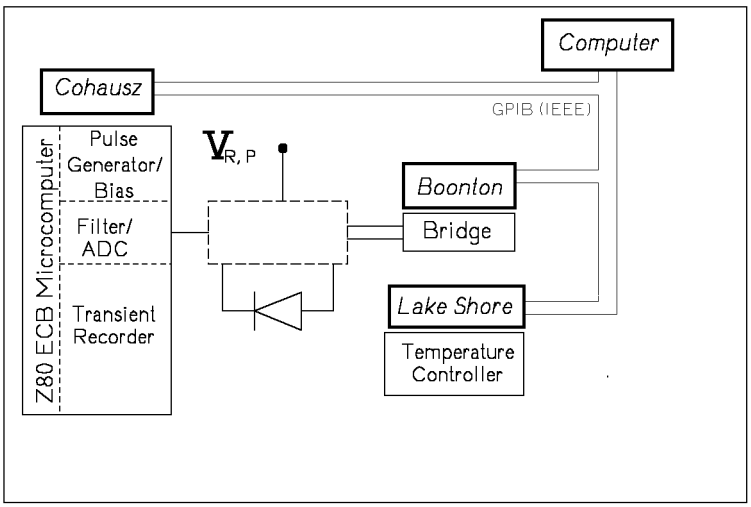

Figure 5.4: DLTS set-up, the Z80 micro computer controls the communication between pulse generator, transient recorder and filter. The dashed box contains a de-coupling circuit.

The software package is divided into three parts. One part controls the measurement, e.g. the temperature ramping, the second part contains the features for analysis and the third part allows the simulation of measurements with given level parameters ($\Delta E_T, \sigma, n_T$). The last feature is a very helpful tool in deconvoluting peaks which are originating from more than one level. The simulation takes into

[3] Made by Dr. Ludwig Cohausz, Halbleitermesstechnik GmbH, Moosburg.

account the exact parameters of the measurement, e.g t_w, dead-time of the bridge and the binning of the transient.

The TSC-measurements were performed with a set-up which equals that used for the IV-measurements, except that the *Lake Shore* temperature controler was added. The current injection was limited either using the K487 to 2 mA or 21 μA respectively, or by connecting resistors in series.

5.4 Cooling and Tempering

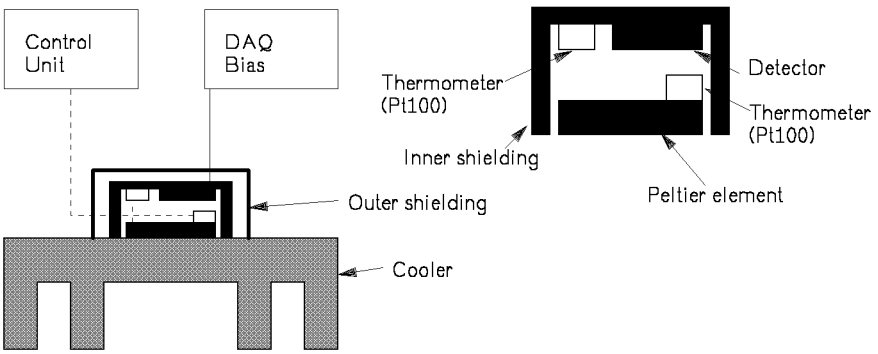

Figure 5.5: The cooling system with Peltier device. The inner shielding consists of a PE cover and a copper foil.

Cooling Peltier devices were used to observe the long term behaviour in the temperature range between 0°C and 20°C .

The main performance requirement of the long term cooling system was to ensure continuous operation independent of the public power network, e.g. during the transport from the irradition facility in Braunschweig back to the laboratory in Hamburg. The solution was found in using Peltier devices with a battery buffered power supply, which made it possible to run the system for 24 hours without external power supply.

The Peltier devices were mounted on a cooler to lead off the heat from the warm side of the device. The samples were mounted on a G10 board, which was fixed at the PE cover opposite to the cool side (see fig. 5.5). The distance between samples and Peltier devices was about 1 mm. The inside of the cover was coated with a copper foil for electrical shielding. The thermometer fixed at the Peltier device was used to control the temperature, that fixed at the G10 board was used to measure the temperature of the samples. The temperature difference was found to be about 5°C. In order to monitor annealing effects at three different temperatures three identical cooling systems were built[4]. The temperatures at the cold side of the Peltier devices were 0°C, 5°C, respectively 10°C, and corresponding at the G10

[4]but connected to one power supply.

board with the samples 6°C, 10°C, and 14°C. The sample temperature could be kept constant within 1°C. Further details can be found in [103].

The DLTS and TSC measurements were performed either on a closed cycle helium cryostat from *CTI-Cryogenics* [104] or on a nitrogen cooled cryostat from *AME* [105]. Both systems were mounted in chambers, which could be evacuated to ensure heat-insulation against the room temperature environment. A schematic diagram of both cryostats is shown in fig. 5.6.

A hot stage has been installed at top of the cold head of the helium cryostat in order to enable controlled heating. The hot stage consisted of a gold-plated copper plate, which was mounted on sapphire collumns to promote the heat (cold) flow and to avoid electrical contact with the cold head, a thermometer (silicon diode DT 470) and a heating resistor (R = 25 Ω and P = 25 W). The plate provided the electrical contact for the rear electrode of the samples. The front contact was a spring needle. The guaranteed accuracy of the diode thermometer was ± 1 K in the temperature range between 100 K and 305 K, respectively ± 0.5 K in the range below 100 K. Both, the thermometer and the heating resistor were connected to a temperature controller DRC 91 CA from *Lake Shore* [106]. The minimum temperature achievable was about 20 K and the maximum heating rate was 1-2 K/s. A complete cool-down and heat-up cycle lasted about half an hour.

The AME cryostat has an integrated temperature controller. The temperature was regulated by variation of the gas (N_2) flow in combination with two heating resistors. The thermometer, a thermoelectric couple which determined the temperature with an acuracy of ± 1 K and the sample were mounted on different sheets of molybdenum. A kapton foil between the cooling block and the molybdenum served

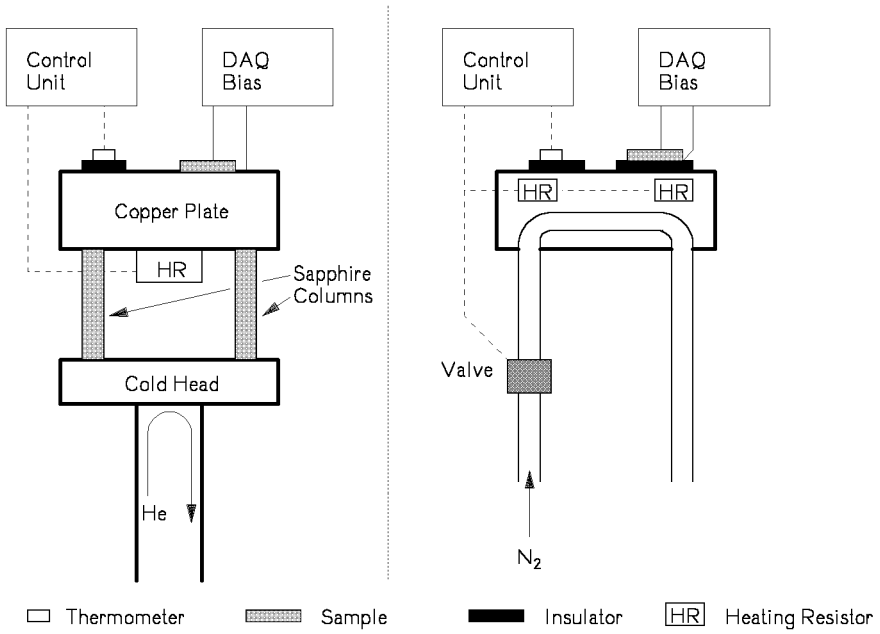

Figure 5.6: Left : Helium cryostat, and right : nitrogen cryostat.

as an electrical insulator. A probe needle was used to contact the front electrode, while the sheet molybdenum provided the contact at the rear side. The minimum temperature was limited to about 80 K. The heating rate was comparable to that of the helium cryostat. However, a complete cool-down and heat-up cycle lasted only about 15 min, not only because the minimum temperature is 60 K higher, but also due to faster cooling.

Comparing the DLT-spectra of one probe [5] recorded on both cryostats it was found that the deviation of the measured temperatures of both cryostats is smaller than 0.5 K.

After irradiation some samples were stored in a refrigerator (deep freeze) at about -25°C in order to suppress annealing effects.

Tempering Two Heraeus furnaces and a vacuum oven were used to perform the heat treatment experiments. The temperature could be kept constant within a range of 0.5 K. The temperature was measured with a Pt100 platinum- resistor and a *Keithley 195A*. If samples on a chip carrier were tempered, the Pt100 was also placed on a similar carrier. After the heat treatment the samples were cooled down very fast by blowing nitrogen. The samples without carrier were placed on a block of brass, which had been heated up before. Thus due to their small heat capacity the samples reached rather quickly the chosen temperature. The thermometer was placed in the same block. A quick cool-down was realised in a similar way. The sample was placed on a block, which was kept at room temperature.

[5] made of GaAs

Chapter 6

Radiation Induced Change of Detector Properties

6.1 Results on Effective Doping Concentration

6.1.1 Introduction

The neutron fluence dependence of the effective doping concentration N_{eff} as determined from the depletion voltage V_{fd} (see eq. 2.25) is shown in fig. 6.1. For low fluences a non-linear decrease of N_{eff} can be observed which is assumed to be due to donor-removal, i.e. those phosphorus atoms which combine with vacancies to form V-P centres do not contribute to the donor concentration anymore (see e.g. [16, 107, 108]). Acceptor-removal is assumed to be negligible, because the corresponding defect (V-B centre) anneals out very rapidly at room temperature (see e.g. [53]). At $\Phi \approx 10^{12}$ cm^{-2} N_{eff} drops close to zero and then increases linearly with fluence. The latter effect is explained as generation of acceptor-like states in proportion to the fluence. Thus the fluence dependence can be summarised by the following formula [109] :

$$N_{eff}(\Phi) = N_{D,0} \exp(-c_D \Phi) - N_{A,0} - b_A \Phi, \tag{6.1}$$

with $N_{D,0}, N_{A,0}$ being the initial phosphorus and boron concentrations respectively, c_D is the removal rate, b_A the generation rate of the acceptor-like states, and Φ the fluence. b_A has been found to be equal for n- and p-type material [76]. Values of the parameters c_D and b_A determined by other authors are summarised in tab. 6.1. The dependence of the effective doping concentration on proton fluence can also be described by eq. 6.1 [108, 78].

Because at a certain fluence the acceptor concentration exceeds the donor concentration, the material undergoes the so-called *type inversion* which has been seen after electron irradiation by Sigfridsson and Lindström [110] for silicon in general, and especially for silicon detectors by Wunstorf et al. [109] and Pitzl et al. [108]. As long as $N_{eff} > 0$ the material is called n-type and if $N_{eff} < 0$ it is p-type. However, it has to be clarified that only the effective space charge changes from positive to negative. If the resistivity, i.e. the density of electrons or holes, is measured in thermal equilibrium silicon is found to become intrinsic with increasing fluence [111, 112] because the Fermi-level adjusts close to midgap [111, 113]. Experimental

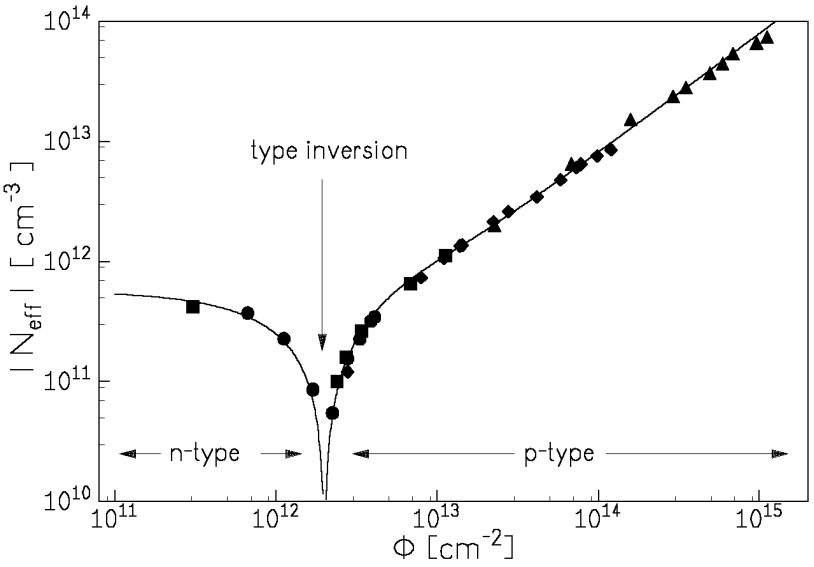

Figure 6.1: Effective doping concentration as function of fluence after correction for self annealing. The solid line is a fit according to eq. 6.1 [109].

$N_{A,0}$ [10^{11} cm^{-3}]	c_D [10^{-13} cm^2]	b_A [cm^{-1}]	Conduction type	Energy [MeV]	Ref.
2.4	3.54 $\pm$ 0.02	0.079 $\pm$ 0.006	n	1 (eq.)	[36] $*$
-	1.87 $\pm$ 0.04	0.073 $\pm$ 0.008	n	$\approx$ 1	[76] $*$
-	1.38 $\pm$ 0.07	0.063 $\pm$ 0.009	p	$\approx$ 1	[76] $*$
1.5	0.47 $\pm$ 0.01	0.031 $\pm$ 0.002	n	$\approx$ 1	[78] †

Table 6.1: Parameters for donor removal (c_D) and acceptor creation (b_A) from different neutron irradiation experiments. $*$: corrected for self annealing, † : 1 day annealing, Note that $N_{A,0}$ is also a result of a fit according to eq. 6.1.

evidence for the type inversion is given by charge collection measurements which show that the SCR starts to grow from the rear side of the detector after type inversion [114, 115, 116]. Eremin found that the sign of the space charge changes again from negative to positive at very low temperatures [117].

The time dependence of the depletion voltage for an inverted and a not inverted sample is shown in fig. 6.2. The obvious difference of the time behaviour can be interpreted consistently by defining a quantity ΔN_{eff} [36]:

$$\Delta N_{eff}(\Phi, t) = N_{eff,0} - N_{eff}(\Phi, t), \tag{6.2}$$

$$N_{eff}(\Phi, t) > 0 \qquad \text{for n-type}, \tag{6.3}$$

$$N_{eff}(\Phi, t) < 0 \qquad \text{for p-type}, \tag{6.4}$$

which is the difference of the effective doping concentration before irradiation and its actual value at time t after irradiation with fluence Φ.

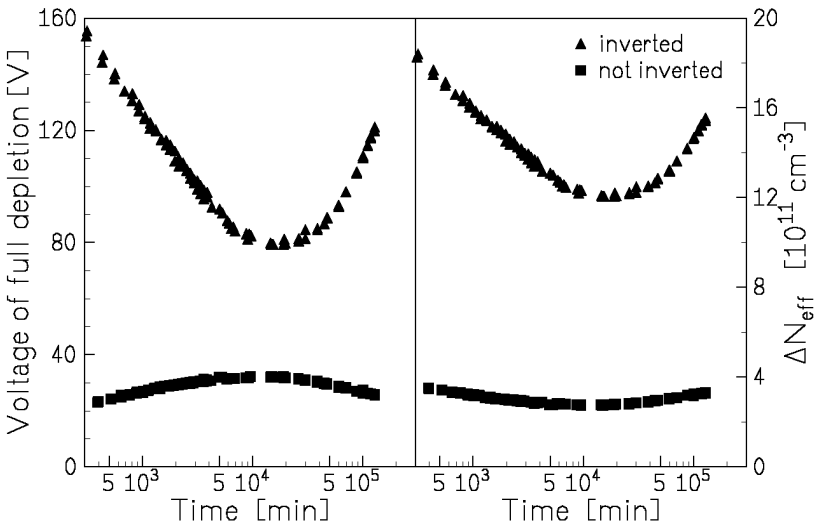

Figure 6.2: Left : voltage for full depletion as function of time, right : ΔN_{eff} as function of time. Not inverted : $\Phi = 3.13{\cdot}10^{12}$ n cm^{-2} (941G18), inverted : $\Phi = 3.56{\cdot}10^{13}$ n cm^{-2} (941G30).

For both cases it can be seen in fig. 6.2 that a period of annealing is followed by an increase of ΔN_{eff} [118] which will be called *reverse annealing* in the following. In the literature this phenomenon is sometimes also called anti-annealing [108]. The short term annealing has been investigated by Wunstorf [36]. Assuming the annealing to be a subsequent first order decay of several defects she used a sum of exponential functions to parametrise the time behaviour and obtained 6 pairs of amplitude A_i and time constant τ_i (see tab. 6.2) from the following equation :

$$\frac{\Delta N_{eff}(t)}{\Delta N_{eff}(0)} = \sum_{i=1}^{6} A_i \exp\left(\frac{-t}{\tau_i}\right). \tag{6.5}$$

Time Constant τ_i [min]	Relative Amplitude A_i
$(9.40 \pm 0.80)10^0$	0.214 ± 0.030
$(6.87 \pm 0.14)10^1$	0.262 ± 0.007
$(3.43 \pm 0.12)10^2$	0.228 ± 0.008
$(4.00 \pm 0.04)10^3$	0.079 ± 0.002
$(7.52 \pm 0.02)10^4$	-0.107 ± 0.001
∞	0.417 ± 0.004

Table 6.2: Annealing parameters of the effective doping concentration according to eq. 6.5 [36]

The negative amplitude has been introduced to describe the first part of the reverse annealing. In the following section the total reverse annealing will be modelled using data taken from isothermal tempering experiments.

6.1.2 The Reverse Annealing

6.1.2.1 Comparison of first and second order approach

If the annealing of ΔN_{eff} is interpreted as a reduction of the space charge, then the reverse annealing has to be regarded as a process of space charge generation, e.g. defects X being neutral in the SCR transform to defects Y which are charged. In case of a transformation of one defect X to one defect Y ($X \Rightarrow Y$) for the concentrations yields :

$$N_{X,0} = N_{Y,\infty} = N_X(t) + N_Y(t), \tag{6.6}$$

where $N_{X,0}$ is N_X at $t = 0$ and $N_{Y,\infty}$ is N_Y at $t = \infty$, and thus

$$N_Y(t) = N_X(t = 0) - N_X(t). \tag{6.7}$$

The same expressions as given in eqs. 6.6 and 6.7 can be used for the case of two neutral defects X_1 and X_2 combining to Y (X_1+$X_2 \Rightarrow Y$) if both are present in similar concentrations (and the indices are omitted, see sec. 3.2). Since the change of V_{fd} during the reverse annealing is caused by the increase of Y, it is useful to describe the time dependence in terms of $N_Y(t)$. Thus one gets for the time dependence either in first order case from eq. 3.6

$$N_Y(t) = N_{X,0}(1 - \exp(-\hat{k}t)), \tag{6.8}$$

or in case of second order from eq. 3.12

$$N_Y(t) = N_{X,0}\left(1 - \frac{1}{1 + N_{X,0}\tilde{k}t}\right). \tag{6.9}$$

Because the annealing has been described very successfully by the first order approach, it is obvious to use it for the reverse annealing as well. However, as can be seen in fig. 6.3 the data are much better fitted by the assumption of a second order process using eq. 6.9. It is noteworthy that the number of free parameters is the same in both cases. It may be possible to improve the first order fit by assuming a sum of exponential functions as used for the annealing. But striking evidence for at least one second order process [1] to be responsible for the reverse annealing is shown in fig. 6.4, where the reverse annealing of two samples with different concentrations $N_{y,\infty}$ is plotted. The reverse annealing of the sample with the higher value of $N_{y,\infty}$ is significant faster than that with the lower concentration. It can be seen clearly how the half-life period depends on the concentration as it is characteristic for a second order process (see eq. 3.14). It is impossible to fit the concentration dependent behaviour to a sum of exponential functions.

[1] or any other concentration dependent process